Available online at www.sciencedirect.com
SCIENCE DIRECT®
PERGAMON
International Journal of Multiphase Flow 29 (2003) 219–247
International Journal of Multiphase Flow
www.elsevier.com/locate/ijmulflow

Experimental and numerical investigation of liquid channel flows with dispersed gas and solid particles

Günter Brenn [*,1], Heiko Braeske, Goran Živković, Franz Durst

Lehrstuhl für Strömungsmechanik, Friedrich-Alexander-Universität Erlangen-Nürnberg, Cauerstraße 4, 91058 Erlangen, Germany

Received 31 July 2000; received in revised form 18 July 2002

Abstract

Two-dimensional single-, two- and three-phase channel flows are investigated experimentally and numerically at the Reynolds numbers 1500, 6500 and 13,000. Local velocities of the continuous liquid and velocities and sizes of the dispersed gaseous and solid phases are measured separately with a phase-Doppler anemometer. Volume concentrations of the dispersed phases were 0.66% for gas bubbles and 0.054% for solid particles. Numerical simulations of the flow were performed with an Euler–Lagrangian model. The model included the relevant physical effects, namely phase interaction, particle dispersion by turbulence, lift forces on the particles, and particle–wall collisions. Comparisons between the measured and calculated data yield good agreement for the liquid and bubble velocity profiles and the bubble size and solid phase distributions. The turbulence levels in the liquid flow from measurement and computation agree well. Bubbles reduce the turbulence level slightly. With increasing Reynolds number the influence of bubbles on the liquid velocity decreases, while the influence of turbulence on the particle motion increases.

Keywords: Multiphase channel flow; Turbulence; Bubbles; Solid particles; Model; Experiment

1. Introduction

Flows with a continuous liquid phase and a dispersed gas and/or solid phase are found widely spread in process engineering. Examples for applications are mineral oil conveying and

* Corresponding author. Fax: +49-9131-8529503.
E-mail address: brenn@fluidmech.tu-graz.ac.at (G. Brenn).
[1] Present address: Graz University of Technology, Institute of Fluid Mechanics and Heat Transfer, 8010 Graz, Austria.

0301-9322/03/$ - see front matter
PII: S0301-9322(02)00133-7

processing, where the oil contains dispersed water drops, gas bubbles and solid particles, biochemical processes with flocculation materials floated by bubbles, and gas–liquid reactions with participation of a solid particulate catalyst.

Flows with a dispersed phase in a continuum are influenced by the interaction between the phases. Contrary to the continuous phase where information about local characteristics of the fluid is transported by the molecular interaction through pressure waves and diffusion, in the dispersed phase there is no analogy for the fluid pressure, and information is transported between bubbles or particles through the conveying fluid. Due to their different histories, there are local differences between hydrodynamic properties of bubbles and solid particles, which is not the case for the continuous phase. There are also phenomena in the dispersed phase with the characteristics of diffusion, caused mainly by the turbulent fluctuations in the continuous phase.

Mathematical treatment of multidimensional multiphase flows for simulating these phenomena is complicated and not yet solved. The exact approach for modelling convection and diffusion processes in multiphase flows requires the knowledge of turbulent characteristics as fluctuation velocity components, autocorrelation functions and Lagrangian integral scales of turbulence. These characteristics are not known for multiphase flows even in the simplest cases. That is why the only possible practical approach is to develop physical and mathematical models closing the problem by using assumptions on the characteristics of the involved phenomena, or by introducing empirical correlations. Enhanced physical knowledge is required to develop improved multiphase models. It is a big challenge to overcome the closure problems between the flow equations of the different phases. Many details about forces on the phases and their interaction are still unknown. There is also a lack of knowledge about the influence of the dispersed phases on the turbulent velocity fluctuations in the continuous phase which is necessary for improving turbulence models. To obtain insight into details of the flow, e.g. the slip velocity or the wall shear stress, the separate measurement of local flow properties of the different phases is essential. Important phenomena are phase separation and spatial phase re-distribution. Remarkable differences in the phase distributions were found for upward and downward flow and for positive and negative buoyant particles, e.g. by Serizawa and Kataoka (1987), Lahey (1990), and Nakoryakov and Kashinsky (1995). Lopez de Bertodano et al. (1994) analysed phase separation and phase redistribution phenomena using two-fluid models.

For modelling the dispersed phase, either the Eulerian or the Lagrangian approach can be used. The Eulerian approach treats the dispersed phase like a fluid. Its main advantage is that it is less time consuming on the computer than the Lagrangian approach. An example of successful two-phase flow modelling by the Eulerian approach is the work of Mostafa and Elghobashi (1985). The Lagrangian approach is closer to the physical reality and yields information necessary for an accurate prediction of particle motion in the turbulent field. For this reason it has been chosen for the present work.

The theoretical basis for phase interaction was established by Migdal and Agosta (1967). According to their model, solid particles, drops and bubbles are treated as sources of mass, momentum and energy in the fluid, represented by source terms in the equations of change. Crowe et al. (1977) used this idea to develop the Particle-Source-in-Cell (PSI-CELL) model. In many models developed later, special attention was given to some particular phenomena in multiphase flows. Rubinow and Keller (1961) developed a theoretical expression for the lift force which acts on a sphere rotating in a viscous fluid. Saffman (1965) modelled the motion of a sphere near the

wall, where the influence of the fluid velocity gradient on the sphere motion was taken into account. Matsumoto and Saito (1970a) modelled particle–wall collisions and investigated the role of wall roughness in preventing particle sedimentation. Wall roughness was modelled by a periodic sinusoidal function, with its amplitude representing the roughness height. Particle non-sphericity was accounted for by treating the particles as ellipsoids. Tsuji et al. (1985) developed a two-phase model for the flow through a horizontal tube, taking into account the Magnus lift force. Milojevic (1990) modelled the effect of fluid turbulence on the dispersed phase, taking into account the crossing-trajectories effect. Sommerfeld and Zivkovic (1992), similar to Oesterle and Petitjean (1993), developed a model in which they simulated wall roughness by the stochastic change of the wall inclination in the model. They also developed a model for particle–particle collisions. The collisions were regarded as a stochastic event, similar to collisions between gas molecules, which can be described by the kinetic theory of gases.

In order to validate such models, reliable measurement data are necessary. In the last decade efforts were made to develop non-intrusive techniques for separate measurement of velocity profiles of the different phases. Since laser-Doppler anemometry (LDA) became a reliable method for accurate velocity measurements in single-phase flows, there were many attempts to apply it also to multiphase flows. Lee and Yang (1989) carried out LDA measurements in three-phase flows discriminating between the dispersed phases by an additional photodiode. Sheng and Irons (1991) combined LDA with an intrusive electrical probe to determine the phase of the signal measured by LDA. Velidandla et al. (1996) measured liquid and gas bubble velocities sequentially, discriminating the LDA signals by the amplitude since bubbles scatter more intense light than the seeding particles in the liquid. Vassallo et al. (1993) introduced an LDA probe which utilised a retroreflector to collect the forward scattered light with a backscatter probe. Two phases were measured simultaneously, measuring forward scattered light from tracers for the liquid phase and backward scattered light from bubbles. Recently Vassallo and Kumar (1999) carried out simultaneous measurements of liquid and gas velocities in an air–water duct flow with LDA using an amplitude discrimination for eliminating bubble signals from forward scattered light and a limitation of gain to suppress the collection of liquid signals with a backscatter probe. A combination of LDA and electrodiffusional techniques was applied by Kashinsky and Timkin (1999) to an upward bubbly two-phase flow. The local mean velocities of the liquid were measured with the intrusive electrodiffusional method, while the local bubble size and velocity were measured with a specially adapted LDA. From the mean profiles the slip velocity was calculated.

An extension of LDA for measuring the size of spherical particles together with their velocity at defined locations in the flow field is phase-Doppler anemometry (PDA). In experiments like the ones presented here, these data can be obtained for up to three phases separately. From the measured data, local concentrations of the dispersed phases can then be calculated, and slip velocities between the phases are easily obtained. Also Reynolds stresses and turbulence intensities can be readily extracted from the measurement data for the continuous phase. Brenn et al. (1994) presented improved PDAs for multiphase flows which allow for a phase discrimination by the dominant light scattering mechanism. Hardalupas et al. (1995) presented an evaluation of PDA for measurements of bubbles. Braeske et al. (1998a,b) presented an extended PDA for three-phase flows and discussed first results.

Hetsroni (1989) gave a review on particle–turbulence interaction, where he limited the discussion to solid particles with sizes between 0.01 and 3 mm. He suggested that particles with

Reynolds numbers below 400 cause suppression of turbulence, while particles with higher Reynolds numbers cause enhancement of turbulence due to wake shedding. In agreement with these results, Braeske et al. (1998b) found a damping influence of solid particles on the velocity fluctuations in the liquid carrier phase. Tran-Cong et al. (1998) and Felton and Loth (1998) investigated experimentally the bubble behaviour in a shear flow and wall effects on bubbles which are important detail phenomena for phase separation.

In the present article PDA data are compared with results from numerical simulations of liquid channel flows without and with dispersed gaseous and solid phases. Section 2 describes set-up and realisation of the experiments. In Section 3 the mathematical model is described. Section 4 presents comparisons of experimental and numerical results. Finally conclusions from the work are drawn.

2. Experimental test rig and technique

An experimental set-up was built to investigate channel flows with a liquid continuous phase and up to two dispersed phases—gas bubbles and/or solid particles. Both bubbles and solid particles will presently be termed "particles" for short. The objects of the measurements were the velocities of all phases and the size distributions and concentrations of the bubbles and solid particles. For the measurements a phase-Doppler anemometer was used.

A sketch of the set-up is depicted in Fig. 1. From the receiving vessel, demineralised water as the liquid phase—without or with solid particles—is pumped through the vertical flow channel and fed back into the vessel. The channel was set up vertical to avoid phase separation due to buoyancy. The gas, which is dispersed into the liquid upstream from the entrance of the channel, exhausts in the receiving vessel, while the solid phase is kept in suspension by a hyperboloid stirrer which generates a uniform concentration.

For driving the flow, a diving motor pump was used. This device is constructed to pump particulate matter, so that it is not destroyed by the solid phase. On the other hand the glass

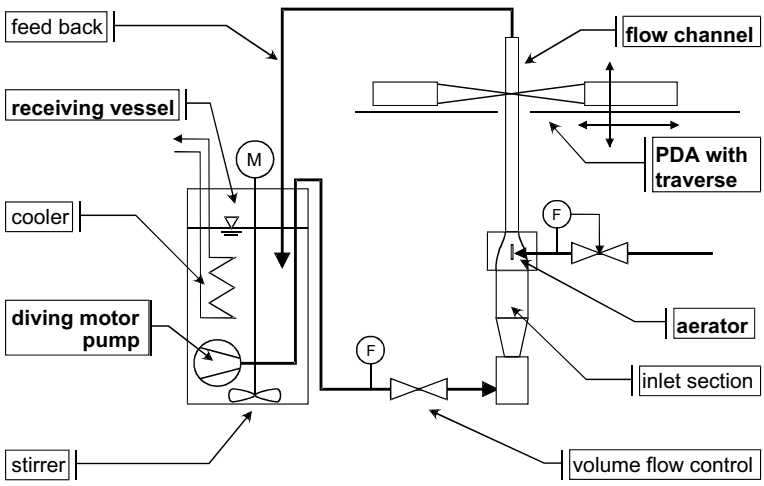

Fig. 1. Scheme of the experimental set-up.

particles are only slightly stressed by the impeller, which ensures that they keep their spherical shape during a long operation time. Since the pump produces waste heat which is transferred to the water in the vessel, the liquid had to be cooled with a heat exchanger connected to the laboratory cooling system. The temperature level of the water was kept constant at the temperature 21 °C with a variation of ±1.5 °C. The liquid flow rate is measured by a flow rate meter FLOWTEC AUTOZERO 2000. It works on a magnetic-inductive principle, which is unaffected by the solid phase. The flow rate is adjusted by a valve downstream from the flow rate meter.

The co-ordinate system is defined in Fig. 2. The x, z plane is the symmetry plane of the channel, with the x-axis oriented upward in the mean flow direction. The co-ordinate origin lies in the entrance plane of the channel. The y-axis is directed along the height of the channel, oriented towards the PDA receiver. The z-axis is oriented against the direction of propagation of the laser beams.

The details of the flow channel are sketched in Fig. 2. The arrangement of the inlet section was taken from Durst et al. (1998). Downstream from the inlet, the flow passes a diffusor with a cross-section of 150×180 mm^2 where the flow is decelerated and tranquillised. Downstream from the diffusor an 80 mm long honeycomb improves the flow uniformity, and a grid of 1 mm mesh size reduces the free-stream turbulence intensity. The contraction chamber reduces the cross-section to the height of the channel and provides a uniform plane flow. The test section of the channel has a cross-section of $H \times B = 15 \times 180$ mm^2. The length of the channel is 900 mm. The ratio H:B of 1:12 ensures two-dimensional flow in the centre of the channel width. The test section was built of four bonded glass plates in a frame of aluminium with the length of the whole channel in order to have optical access from two directions, to avoid critical sealing joints, to have hydraulically smooth surfaces and to minimise disturbances to the flow. At the entrance of the channel two plates were mounted along the broad side to trip the developing boundary layers. The plates had a thickness of 2 mm and reached 1 mm into the flow. The blocked height was therefore 13.3% of the channel height. According to Durst et al. (1998), fully developed flow conditions are reached very rapidly at a Reynolds number $Re_C \approx 4000$ for a trip blockage ratio of 10%, where $Re_C = U_c H/\nu$ with the centre line flow velocity U_c and the channel height H. Below $Re_C \approx 1800$, the turbulence level is about 0.007 and constant. In every case some downstream length in the channel is necessary for the velocity profile to be developed. From the Blasius expression $\delta = 5\sqrt{x\nu/U}$ for the thickness of the boundary layer δ in the x direction along a plate, the criterion for the cross-section where the flow is fully developed is $x/H = 0.01\,Re_C$. From this criterion it follows that cross-sections up to $x/H = 50$ fall into the region of not fully developed flow. Since this estimate is not quantitatively applicable for our channel flow, however, we assume that even at our measurement position $x = 750$ mm ($= 50H$) farthest downstream from the channel entrance, the flow even with tripped boundary layer is not fully developed for the Reynolds numbers $Re = U_e H/\nu = 1500$, 6500 and 13,000 in the present experiments, formed with the flow rate-equivalent velocity U_e. Measurement and calculation results in Section 4 will confirm this. For the scope of our work, the fully developed state of the flow is not needed.

The aerator was placed in the contraction zone. The shape of the sparger body was chosen so as to minimise disturbances to the flow. The air supplied from a pressurised line in the laboratory emerged from a microporous polyurethane membrane (pore diameter about 30 μm) clamped inside the aerator body behind two shifted rows of holes with a diameter of 4 mm. The air flow rate was controlled by a Bronkhorst mass flow controller. The aerator creates bubbles with a size

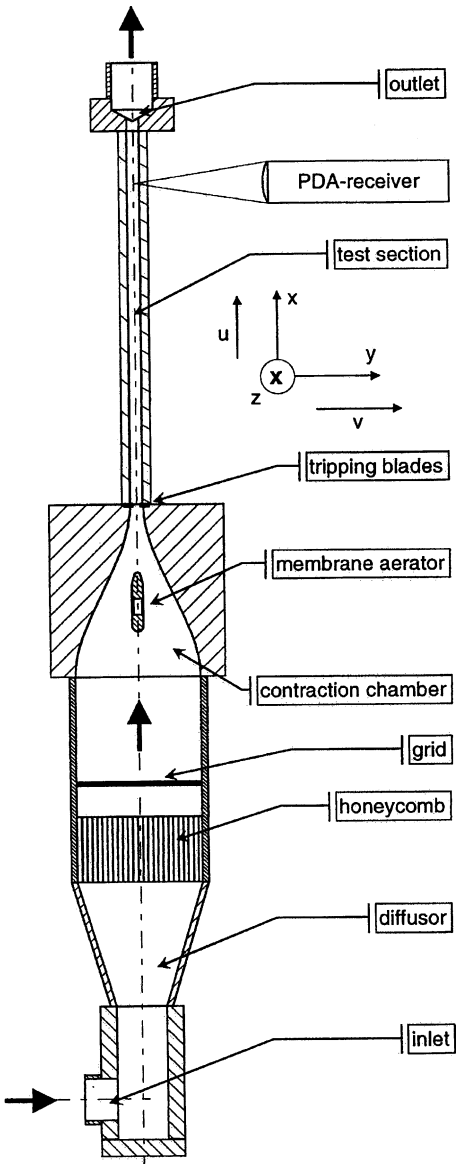

Fig. 2. Flow channel with inlet, test section and outlet.

distribution at the entrance of the test section which could not be measured due to limitations of the optical access. From measurements in a bubble column equipped with a similar membrane aerator, however, it is known that the bubbles emerging from the membrane have a mean diameter of about 400 μm. In turbulent flow, the bubbles enter the test section close to the centre of the channel. In laminar flow, large bubbles move fairly straight upwards, while small bubbles may be forced towards the channel centre due to shear forces. By this mechanism a separation of bubbles by their size occurs, where mainly the small bubbles reside in the centre of the channel,

and the large bubbles rise close to the wall. The produced bubbles moved through the channel within a very short time, so that practically no coalescence could occur.

The flow measurements were performed with a PDA from Dantec. The PDA enables measurements of two velocity components and the size of spherical bubbles and solid particles. From the measurement data we obtain also information about solid particle/bubble concentration and details of the time dependent behaviour of the flow.

The PDA is operated with a 300 mW argon-ion laser. The light enters the transmitting optics, separated by colours. The green (514.5 nm) and blue (488.0 nm) pairs of beams are aligned in the x,z and y,z planes, respectively, and form the measurement volume with a diameter of 140 μm. The two pairs of beams permit the measurement of two velocity components. In the near wall region one blue beam in the y,z plane is blocked by the wall, and thus only the vertical velocity can be obtained there. The scattered light enters the receiving unit and reaches the four photomultipliers via a slit aperture and colour separating prisms. The receiving unit was installed at the geometric scattering angle of 73°. Since its optical axis is then inclined relative to the normal direction on the side window by an angle of 17°, the effective scattering angle becomes 77.3°. For this angle the dominant scattering mechanism is reflection for both bubbles and solid particles, and thus the measurement of all phases can be performed with the same phase–diameter relationship, independent of the particle refractive index. The configuration data of the PDA are listed in Table 1.

The measurement data for each detected and validated particle are arrival and transit times, two velocity components and diameter. The statistical evaluation is performed by Dantec's software package SIZEWARE, which provides probability density distributions, mean values and higher order moments, as well as derived quantities like Reynolds stresses and volume fluxes. For

Table 1
Optical configuration of the Dantec PDA system

Transmitting optics	
Laser power	300 mW
Wave length	514 nm (U_x/D)/488 nm (U_y)
Focal length	310 mm
Beam separation	10 mm
Beam diameter	1.4 mm
Polarisation	Parallel (0°) without glass particles Perpendicular (90°) with glass particles
Fringe spacing	16.0 μm (U_x)/15.1 μm (U_y)
Number of fringes	9
Probe volume diameter	145 μm (U_x)/138 μm (U_y)
Probe volume length	≈11.5 mm
Light intensity in probe volume	1.95×10^6 W/m^2
Shift frequency	40 MHz
Receiving optics	
Scattering angle φ	77.3°
Detector elevation adjust	0.0, 0.74, 1.0 or 2.0 mm
Focal length	310 mm
Phase factor 1–2	−0.6027, −0.7888, −0.7940 or −0.9693 °/μm
Phase factor 1–3	−0.1766, −0.3469, −0.3798, or −0.4846 °/μm

achieving statistical certainty, 6000–14,000 samples are acquired at each measuring position in the flow.

The PDA is mounted on a base platform, which can be manually relocated in the x direction along the channel length. In the horizontal y,z plane, the platform is traversed by electric motors. The position-dependent shift of the focus points in the liquid, discussed by Braeske et al. (1998b), is compensated by a fourth traverse along the optical axis of the receiving optics unit.

For velocity measurements in the liquid phase, tracer particles were added to the water. Silver coated hollow glass spheres with a density of 1.4 g/cm^3, a mean diameter of 10 μm and a size distribution between 2 and 30 μm were used. For the given particle and water characteristics, the particle hydrodynamic response time $\tau_p = \rho_p D_p^2/(18\mu)$ (with the particle size and density D_p and ρ_p and the liquid dynamic viscosity μ) is about 7.8×10^{-6} s. On the other hand, Kolmogorov's time $\tau_K = L_E^2 Re^{-3/2}/v$ (with the Lagrangian integral turbulence length scale L_E) is, for example for $Re = 12{,}000$, about 1.7×10^{-4} s. This yields the ratio τ_p/τ_K with a value of the order of 10^{-2}, clearly below 1. As a consequence, the particles follow the water velocity very well and can be used as tracers. The solid phase were spherical glass particles with diameters between 124 and 162 μm. Their density was 2184 kg/m^3; the refractive index was 1.519 relative to air. The mass concentration in water was calculated from the added solid mass and the liquid mass inside the whole system. Since the bubbles exhibited diameters above 300 μm, all three phases—tracers, solid glass spheres and bubbles—could be clearly discriminated by the diameter information, which enables the use of the commercial phase-Doppler anemometer without any extension but a diameter-separated data processing.

In order to compare experimental and computational results and to measure an influence of the dispersed phases on the flow behaviour, measurements were first carried out in liquid single-phase flow. Velocity profiles along the y-co-ordinate were measured at three distances downstream from the channel entrance: $x/H = 30$, 40, and 50. These profiles were measured in order to investigate the development of the flow in the main flow direction.

3. Mathematical model of multiphase flows of liquid with bubbles and solid particles

A mathematical model for simulating steady multiphase flows was developed. The liquid phase was treated following the Eulerian approach, i.e. the liquid parameters were defined as functions of spatial co-ordinates. The gas bubble and solid particle phases were treated following the Lagrangian approach, which means that the parameters of every particle are functions of time (Durst et al., 1984). Even though this means that in the equations of particle motion time appears explicitly, the mean characteristics of the dispersed phase in a sufficiently long period of time do not change, so that we can consider them as stationary. As results of this computation, one obtains the fields of mean velocities, turbulent kinetic energy and dissipation rate, pressure drop, and mean velocities and mass concentration for the dispersed phases.

The flow is treated as two-dimensional. The presence of bubbles and particles in the liquid does not confound the two-dimensional character in the experiment, so that a 2-D flow model was enough to yield results which can be validated by comparison with the experiments. Although, in principle, the disperse phases could also be described by a 2-D approach, a 3-D model was developed in order to take into account particle and bubble interactions with the walls.

For the coupling of phases, the PSI-CELL method of Crowe et al. (1977) was chosen. By this method all influences of the dispersed phases on the continuous phase are accounted for through source terms in the equations describing the liquid phase. This could only be done assuming that the total volume of the dispersed phases is small in comparison with the volume of the flow domain. This allows for the treatment of the liquid phase as a Newtonian fluid. In a liquid–solid particle mixture, due to the large particle density (and therefore small particle volume fraction) this is practically always the case. In a liquid–bubble mixture, the gas-to-liquid volume ratio should not exceed some few percent to fulfil this requirement. Although in real devices this is not always the case, in experiments it is often realised to avoid problems with bubble velocity measurements for values above 5%. Since in all measurements presented in this work the bubble-to-fluid volume ratio did not exceed 1%, it can be concluded that, for the purpose of this work, the required conditions for using the PSI-CELL method were fulfilled. A further assumption is that the boundary conditions affect directly only the continuous phase (and the disperse phases through the coupling of phases). By this method the model of the flow of a multiphase mixture is reduced to a single-phase model with source terms to account for the disperse phases.

3.1. Equations of fluid motion

The motion of the fluid is described by the continuity and the Navier–Stokes equations. Turbulence is modelled by the standard k–ε model (Launder and Spalding, 1974; Hinze, 1975; Patankar, 1980). The equations for the liquid flow are

$$\frac{\partial(\rho U_i)}{\partial x_i} = 0 \qquad \text{(continuity)} \tag{1}$$

$$\frac{\partial}{\partial x_j}\left[\rho U_i U_j + \overline{\rho u_i u_j} - \mu\frac{\partial U_i}{\partial x_j}\right] = -\frac{\partial P}{\partial x_i} + S^{\mathrm{p}}_{u_i} \qquad \text{(Navier–Stokes)} \tag{2}$$

$$\frac{\partial}{\partial x_j}\left[\rho U_j k - \frac{\mu_{\mathrm{eff}}}{\sigma_k}\frac{\partial k}{\partial x_j}\right] = P_k - \rho\varepsilon + S^{\mathrm{p}}_k \qquad \text{(turbulent kinetic energy)} \tag{3}$$

$$\frac{\partial}{\partial x_j}\left[\rho U_j \varepsilon - \frac{\mu_{\mathrm{eff}}}{\sigma_\varepsilon}\frac{\partial \varepsilon}{\partial x_j}\right] = \frac{\varepsilon}{k}(C_{\varepsilon 1}P_k - C_{\varepsilon 2}\rho\varepsilon) + S^{\mathrm{p}}_\varepsilon \qquad \text{(turbulent dissipation)} \tag{4}$$

$$\mu_{\mathrm{eff}} = \mu + \mu_{\mathrm{t}} \qquad \mu_{\mathrm{t}} = \frac{C_\mu \rho k^2}{\varepsilon} \qquad P_k = \mu_{\mathrm{eff}}\left(\frac{\partial U_i}{\partial x_j} + \frac{\partial U_j}{\partial x_i}\right)\frac{\partial U_i}{\partial x_j} \tag{5}$$

In these equations U_i denotes the cartesian velocity components, x_i cartesian co-ordinates, P the fluid pressure, k and ε turbulent kinetic energy and dissipation rate, ρ and μ the fluid density and dynamic viscosity, and μ_{t} the turbulent viscosity. Source terms due to the presence of particles are denoted by the superscript p and are given according to Lee and Durst (1982) by the equations

$$S^{\mathrm{p}}_{u_i} = \frac{1}{V_{\mathrm{cv}} t_{\mathrm{tot}}}\sum_n m_n(U_i^{\mathrm{out}} - U_i^{\mathrm{in}} - g_i \Delta t_{\mathrm{cv}}) \qquad S^{\mathrm{p}}_k = \sum_i \overline{u_i S^{\mathrm{p}}_{u_i}} - \overline{u_i}\,\overline{S^{\mathrm{p}}_{u_i}} \qquad S^{\mathrm{p}}_\varepsilon = C_3\frac{\varepsilon}{k}S^{\mathrm{p}}_k \tag{6}$$

Here V_{cv} is the control volume, t_{tot} the total time period covered by the calculation of n parcels, m_n the mass of a parcel, and Δt_{cv} the total time of a parcel spent in the control volume. The term

parcel will be discussed in Section 3.3. The summation is performed over all particles passing the considered control volume in the period t_{tot}. For the k–ε model, the following standard coefficients are used:

C_μ	$C_{\varepsilon 1}$	$C_{\varepsilon 2}$	C_3	σ_k	σ_ε
0.09	1.44	1.92	0.7	1.0	1.3

For solving this system of equations, the control volume method was adopted. The basis of the code was the numerical code CAST for single-phase flow, based on the SIMPLE algorithm, with collocated grid and hybrid scheme. This code was extended by introducing the additional source terms (6) to account for the presence of particles.

The solution of the above set of equations was subject to the boundary conditions at the entrance of the test section—profile of the flow velocity U_x uniform with the value to represent the flow rate, $U_y = U_z = 0$, and turbulence level based on U_x assumed to be 10%—and at the channel walls logarithmic wall functions used to calculate the flow velocity in x direction at the grid level closest to the wall, while representing the wall shear stress correctly. The outflow level was placed far enough downstream to ensure vanishing gradients of the flow parameters in flow direction—presently this downstream distance was taken to be 1 m from the entrance.

3.2. Equations of motion of particles and bubbles

For describing the particle and bubble motion correctly, all significant forces acting during the motion must be taken into account. There are two kinds of such forces—those acting permanently, and those acting as impulses (Ahmad and Goulas, 1980; Durst and Raszillier, 1989; Oesterle and Petitjean, 1993). The origin of the first kind of forces is the presence of the continuous liquid phase and gravity, while the second kind of forces is caused by particle–wall and particle–particle interactions.

For proper calculation of a force acting on some body, it is necessary to know the body shape. In principle the shape of both solid particles and bubbles is irregular. Accordingly, there are some models of particle motion, which take into account the shape of the particles (Matsumoto and Saito, 1970b). In a wide range of other models, however, particles and bubbles are treated as spheres. The motion of bubbles is affected significantly by their shape. Under certain conditions, however, bubbles can also be treated as spheres. These conditions are quantified by the values of the bubble Reynolds number $Re_b = D_b|U - V|/\nu$ and of the Eötvös number $Eo = g|\rho - \rho_b|D_b^2/\sigma$ of the bubbles, with the bubble size D_b, the relative velocity U–V and the density difference ρ–ρ_b between liquid and bubble, the gravitational acceleration g, the kinematic viscosity of the liquid ν and the surface tension σ. For bubbles of air in water, the value of the surface tension is $\sigma = 7.2 \times 10^{-2}$ N/m, the difference between bubble and water velocity $|U - V|$ may be assumed to be O(0.15 m/s), and the size is $D_b \approx$ O(0.4 mm). Thus, $Re_b \approx \mathrm{O}(10^2)$ and $Eo \approx \mathrm{O}(10^{-1})$. According to Clift et al. (1978), bubbles with these characteristics can be treated as spherical. Following this conclusion, the forces acting on the bubbles in the fluid will be modelled assuming spherical bubble shape.

The most important force is the drag force, which is defined by the equation

$$\vec{F}_{\mathrm{D}} = C_{\mathrm{D}} \frac{\pi D_{\mathrm{p}}^2}{4} \frac{1}{2} \rho (\vec{U} - \vec{V}) |\vec{U} - \vec{V}| \tag{7}$$

Here we denote the particle properties with subscript p to mean both bubbles and solid particles. The drag coefficient C_{D} depends on the particle Reynolds number $Re_{\mathrm{p}} = D_{\mathrm{p}} \rho |\vec{U} - \vec{V}| / \mu$, with the particle size D_{p}. Among many expressions for C_{D} which can be found in the literature, the following are the most common and are used in the present calculations:

$$\begin{aligned}
C_{\mathrm{D}} &= \frac{24}{Re_{\mathrm{p}}} \quad Re_{\mathrm{p}} \leqslant 0.2 \\
C_{\mathrm{D}} &= \frac{24}{Re_{\mathrm{p}}} (1 + 0.1 Re_{\mathrm{p}}^{0.99}) \quad 0.2 < Re_{\mathrm{p}} \leqslant 2 \\
C_{\mathrm{D}} &= \frac{24}{Re_{\mathrm{p}}} (1 + 0.11 Re_{\mathrm{p}}^{0.81}) \quad 2 < Re_{\mathrm{p}} \leqslant 21 \\
C_{\mathrm{D}} &= \frac{24}{Re_{\mathrm{p}}} (1 + 0.189 Re_{\mathrm{p}}^{0.632}) \quad 21 < Re_{\mathrm{p}} \leqslant 200 \\
C_{\mathrm{D}} &= \frac{24}{Re_{\mathrm{p}}} (1 + 0.15 Re_{\mathrm{p}}^{0.687}) \quad 200 < Re_{\mathrm{p}} \leqslant 1000 \\
C_{\mathrm{D}} &= 0.44 \quad 1000 < Re_{\mathrm{p}} \leqslant 2 \times 10^5 \\
C_{\mathrm{D}} &= 0.1 \quad Re_{\mathrm{p}} > 2 \times 10^5
\end{aligned} \tag{8}$$

Due to frequent collisions with the walls, the particles can rotate with large angular velocity $\vec{\omega}_{\mathrm{p}}$. In a viscous fluid this rotation induces a lift force and torque, which have to be taken into account in the calculation of the solid particle or bubble motion. Rubinow and Keller (1961) analysed the rotation of a sphere in a viscous fluid with small particle Reynolds number and obtained the following relation for the lift force and torque:

$$\vec{F}_{\mathrm{L}} = \pi \frac{D_{\mathrm{p}}^3}{8} \rho \vec{\omega}_{\mathrm{p}} \times \vec{U} [1 + G(Re_{\mathrm{p}})] \tag{9}$$

$$\vec{T} = -\pi \mu D_{\mathrm{p}}^3 \vec{\omega}_{\mathrm{p}} [1 + g(Re_{\mathrm{p}})] \tag{10}$$

where $G(Re_{\mathrm{p}})$ and $g(Re_{\mathrm{p}})$ are functions of the particle Reynolds number. Rubinow and Keller (1961) proved that, for small Reynolds numbers, these functions could be neglected. They also showed that particle rotation does not influence the drag force and vice versa, so that these effects can be treated separately. In the case of turbulent flow, the rotation of the fluid should also be accounted for. According to Ahmad and Goulas (1980), this can be done by introducing the additional term $1/2 \nabla \times \vec{U}$ into Eqs. (9) and (10), to obtain:

$$\vec{F}_{\mathrm{L}} = \pi \frac{D_{\mathrm{p}}^3}{8} \rho \left(\vec{\omega}_{\mathrm{p}} - \frac{1}{2} \nabla \times \vec{U} \right) \times (\vec{V} - \vec{U}) \tag{11}$$

$$\vec{T} = -\pi \mu D_{\mathrm{p}}^3 \left(\vec{\omega}_{\mathrm{p}} - \frac{1}{2} \nabla \times \vec{U} \right) \tag{12}$$

If there is a velocity gradient in the fluid through which the particle moves, the pressure field around the particle is no more symmetrical, and the resulting drag force deviates from Eq. (7). This effect can be explained by the action of a new force (with the drag force remaining the same as before). This new force was analysed by Saffman (1965), for the case of particle motion through a very viscous fluid, and for the case of a velocity gradient perpendicular to the direction of motion. The value of the force is relatively small in many cases, but it can be important for small particles in the near-wall regions, where the fluid velocity gradient is high. Saffman derived the force only for two-dimensional motion (particle velocity and velocity gradient in one plane). Žívković (1996) developed a generalisation of the expression of the Saffman force for the three-dimensional case, which reads

$$\vec{F}_{\mathrm{S}} = -1.54 m_{\mathrm{p}} \frac{(\rho\mu)^{1/2}}{\rho_{\mathrm{p}} D_{\mathrm{p}} |\nabla|\vec{V} - \vec{U}\|^{1/2}} \nabla(\vec{V} - \vec{U})^2 \tag{13}$$

with the particle mass m_{p}. Gravitational and buoyancy forces also play an important role for the motion of the disperse phases. Their difference is defined by the equation

$$\vec{F}_{\mathrm{B}} = V_{\mathrm{p}}(\rho_{\mathrm{p}} - \rho)\vec{g} \tag{14}$$

where V_{p} is the particle volume. Due to the solid particle or bubble motion, a part of the surrounding fluid is accelerated, which leads to an additional resistance of the fluid against the particle motion. This effect can be accounted for by introducing the so-called "additional mass" force

$$\vec{F}_{\mathrm{AM}} = c_A V_{\mathrm{p}} \rho \frac{\mathrm{d}}{\mathrm{d}t}(\vec{U} - \vec{V}) \tag{15}$$

According to Odar and Hamilton (1964), the virtual mass coefficient c_{A} is defined as

$$c_{\mathrm{A}} = 1.05 - \frac{0.066}{A_{\mathrm{c}}^2 + 0.12}, \quad \text{where } A_{\mathrm{c}} = \frac{|\vec{U} - \vec{V}|^2}{D_{\mathrm{p}} \left| \frac{\mathrm{d}|\vec{U} - \vec{V}|}{\mathrm{d}t} \right|} \tag{16}$$

is the coefficient of acceleration. When the fluid density ρ is much smaller than the particle density ρ_{p}, the force (15) can obviously be neglected, but in the case of bubble motion it may be significant and was therefore included in the model.

Besides the above mentioned forces, there are also forces due to the pressure gradient, as well as the Basset force, due to the accelerating action of the particle on the fluid. These two terms, however, can be neglected in the present case of steady flow with small differences between particle and fluid velocities.

For solving the equations of particle motion, a semi-analytical approach was adopted. For realising this approach, the whole time interval during which the particle was followed was divided into subintervals. Particle position, velocity and angular velocity were calculated at the end of each subinterval. It was assumed that, during the subinterval, the values of lift, Saffman, and additional mass forces and a factor f_{corr} do not change. The factor f_{corr} accounts for deviations of C_{D} from the Stokes expression $C_{\mathrm{D}} = 24/Re_{\mathrm{p}}$ and is defined by the expressions in brackets in Eqs. (8). For this assumption to be valid, the time subintervals must be chosen short enough.

Regarding the forces as constant during one subinterval, the differential equations for particle motion read

$$\frac{\mathrm{d}\vec{V}}{\mathrm{d}t} = \frac{\pi D_\mathrm{p} \mu C_\mathrm{D} Re_\mathrm{p}}{8 m_\mathrm{p}} (\vec{U} - \vec{V}) + \vec{g}\left(1 - \frac{\rho}{\rho_\mathrm{p}}\right) + \frac{\vec{F}_\mathrm{L} + \vec{F}_\mathrm{S} + \vec{F}_\mathrm{AM}}{m_\mathrm{p}} \tag{17}$$

$$I_\mathrm{p} \frac{\mathrm{d}\vec{\omega}_\mathrm{p}}{\mathrm{d}t} = \vec{T} \tag{18}$$

where I_p is the angular moment of inertia of the particle. These equations can be solved analytically to obtain the three cartesian components of the particle velocity

$$V_x = U_x - (U_x - V_{x0}) \exp\left(-\frac{\Delta t}{\tau_\mathrm{p}}\right) + \frac{3}{4}\frac{\rho}{\rho_\mathrm{p}} \tau_\mathrm{p} \left[1 - \exp\left(-\frac{\Delta t}{\tau_\mathrm{p}}\right)\right] \cdot \left\{ \frac{F_{\mathrm{S}_x} + F_{\mathrm{AM}_x}}{m_\mathrm{p}} - g\left(1 - \frac{\rho}{\rho_\mathrm{p}}\right) + (V_z - U_z)\left[\omega_{\mathrm{p}_y} - \frac{1}{2}\left(\frac{\partial U_x}{\partial z} - \frac{\partial U_z}{\partial x}\right)\right] - (V_y - U_y)\left[\omega_{\mathrm{p}_z} - \frac{1}{2}\left(\frac{\partial V_y}{\partial x} - \frac{\partial V_x}{\partial y}\right)\right]\right\} \tag{19}$$

$$V_y = U_y - (U_y - V_{y0}) \exp\left(-\frac{\Delta t}{\tau_\mathrm{p}}\right) + \frac{3}{4}\frac{\rho}{\rho_\mathrm{p}} \tau_\mathrm{p} \left[1 - \exp\left(-\frac{\Delta t}{\tau_\mathrm{p}}\right)\right] \cdot \left\{ \frac{F_{\mathrm{S}_y} + F_{\mathrm{AM}_y}}{m_\mathrm{p}} + (V_x - U_x)\left[\omega_{\mathrm{p}_z} - \frac{1}{2}\left(\frac{\partial U_y}{\partial x} - \frac{\partial U_x}{\partial y}\right)\right] - (V_z - U_z)\left[\omega_{\mathrm{p}_x} - \frac{1}{2}\left(\frac{\partial V_z}{\partial y} - \frac{\partial V_y}{\partial z}\right)\right]\right\} \tag{20}$$

$$V_z = U_z - (U_z - V_{z0}) \exp\left(-\frac{\Delta t}{\tau_\mathrm{p}}\right) + \frac{3}{4}\frac{\rho}{\rho_\mathrm{p}} \tau_\mathrm{p} \left[1 - \exp\left(-\frac{\Delta t}{\tau_\mathrm{p}}\right)\right] \cdot \left\{ \frac{F_{\mathrm{S}_z} + F_{\mathrm{AM}_z}}{m_\mathrm{p}} + (V_y - U_y)\left[\omega_{\mathrm{p}_x} - \frac{1}{2}\left(\frac{\partial U_z}{\partial y} - \frac{\partial U_y}{\partial z}\right)\right] - (V_x - U_x)\left[\omega_{\mathrm{p}_y} - \frac{1}{2}\left(\frac{\partial V_x}{\partial z} - \frac{\partial V_z}{\partial x}\right)\right]\right\} \tag{21}$$

Subscript '0' denotes the value at the beginning of the time subinterval Δt. The quantity τ_p is the hydrodynamic particle response time defined as

$$\tau_\mathrm{p} = \frac{D_\mathrm{p}^2 \rho_\mathrm{p}}{18 f_\mathrm{corr} \mu} \tag{22}$$

For the angular velocity we have

$$\vec{\omega}_\mathrm{p} = \frac{1}{2}\nabla \times \vec{U} + \left(\omega_{p0} - \frac{1}{2}\nabla \times \vec{U}_0\right) \exp\left(-\frac{60\mu}{\rho_\mathrm{p} D_\mathrm{p}^2} \Delta t\right) \tag{23}$$

The last forces to be considered are those by particle–wall and particle–particle collisions acting as impulses. The importance of the latter depends on the frequency of the collisions. The mutual interaction of particles must be taken into account in cases of high particle-to-fluid volume load ratio. There are criterions for determining when this is necessary (Crowe, 1981; Živković, 1996). Briefly, it can be said that, for the regimes considered in this work, the load ratios were far below those which would demand particle–particle collision modelling.

For particle–wall collisions a model of a sphere hitting a smooth wall was developed. Basic assumptions of the model are that the particle shape is not altered by rupture or plastic deformation, that there is a period of particle sliding on the wall surface, that, once a particle stops sliding, it continues to roll along the whole period of contact with the surface, and that friction between the particle and the surface obeys Coulomb's law. The whole collision period can be divided into two parts: (a) a compression period (the particle is elastically compressed), and (b) a recovery period (the particle returns to the state before the collision). Depending on when the particle stops sliding, three types of collisions can be distinguished: collisions where (1) the particle stops sliding in the compression period, where (2) the particle stops sliding in the recovery period, or where (3) the particle slides for the whole period of collision. The occurrence of one of these cases depends on the friction factor f, the restitution coefficient e, and the angle between particle velocity and the collision plane at the instant of collision. The direction of the main flow, the direction normal to the collision plane, and the third direction are called x, y and z, respectively. The conditions for which the three cases are fulfilled are

$$(1)\quad \frac{V_y^{(0)}}{|\vec{V}|} < -\frac{2}{7f} \qquad (2)\quad -\frac{2}{7f} < \frac{V_y^{(0)}}{|\vec{V}|} < -\frac{2}{7f(1+e)} \qquad (3)\quad -\frac{2}{7f(1+e)} < \frac{V_y^{(0)}}{|\vec{V}|}$$

The expressions for the components of velocity and angular velocity are the same for the first two cases, and differ for the third. They read

Cases (1) and (2)

$$\begin{aligned} V_x &= \frac{5}{7}\left(V_x^{(0)} - \frac{1}{5}D_\mathrm{p}\omega_z^{(0)}\right) & \omega_x &= \frac{10}{7D_\mathrm{p}}\left(V_z^{(0)} + \frac{1}{5}D_\mathrm{p}\omega_x^{(0)}\right) = \frac{2V_z}{D_\mathrm{p}} \\ V_y &= -eV_y^{(0)} & \omega_y &= \omega_y^{(0)} \\ V_z &= \frac{5}{7}\left(V_z^{(0)} + \frac{1}{5}D_\mathrm{p}\omega_x^{(0)}\right) & \omega_z &= -\frac{10}{7D_\mathrm{p}}\left(V_x^{(0)} - \frac{1}{5}D_\mathrm{p}\omega_z^{(0)}\right) = -\frac{2V_x}{D_\mathrm{p}} \end{aligned} \tag{24}$$

Case (3)

$$\begin{aligned} V_x &= \varepsilon_x f(1+e)V_y^{(0)} + V_x & \omega_x &= -5\frac{\varepsilon_z f(1+e)V_y^{(0)}}{D_\mathrm{p}} + \omega_x^{(0)} \\ V_y &= -eV_y^{(0)} & \omega_y &= \omega_y^{(0)} \\ V_z &= \varepsilon_z f(1+e)V_y^{(0)} + V_z^{(0)} & \omega_z &= 5\frac{\varepsilon_x f(1+e)V_y^{(0)}}{D_\mathrm{p}} + \omega_z^{(0)} \end{aligned}$$

where

$$\begin{aligned} \varepsilon_x &= \frac{V_x^{(0)} + D_\mathrm{p}\omega_z^{(0)}/2}{\sqrt{\left(V_x^{(0)} + D_\mathrm{p}\omega_z^{(0)}/2\right)^2 + \left(V_z^{(0)} - D_\mathrm{p}\omega_x^{(0)}/2\right)^2}} \\ \varepsilon_z &= \frac{V_z^{(0)} - D_\mathrm{p}\omega_x^{(0)}/2}{\sqrt{\left(V_x^{(0)} + D_\mathrm{p}\omega_z^{(0)}/2\right)^2 + \left(V_z^{(0)} - D_\mathrm{p}\omega_x^{(0)}/2\right)^2}} \end{aligned} \tag{25}$$

3.3. Particle size distribution and notion of the parcel

Since the sizes of solid particles and bubbles play an important role in their motion, their size distribution is also included in the model. Sommerfeld (1987) showed that the log-Gaussian distribution for the particle size yields the best agreement of numerical results with experiment:

$$f(D_\mathrm{p}) = \frac{1}{\sqrt{\pi s^2/2} D_\mathrm{p}} \exp\left(- \frac{(\ln D_\mathrm{p}/D_\mathrm{pm})^2}{2s^2} \right) \qquad s^2 = \ln \frac{D_\mathrm{pm}}{D_\mathrm{pNmax}} \tag{26}$$

In this equation, D_pm and D_pNmax are the mean and the most probable particle sizes, respectively. The standard deviation s is the width of the size distribution in the ensemble of particles. In this work it was assumed that $s^2 = 0.25$.

The Lagrangian approach can follow only a moderate number of particles. The real number of particles in the flow domain, however, is very large. For this reason, the special term 'parcel' of particles was defined. Parcels represent a large bulk of particles with the same size, mass, velocity and position. The model is arranged such that every parcel represents the same mass of a disperse phase. This means that different parcels in general represent different numbers of real particles, depending on the parcel (particle) size. Thus, the distribution of the parcel size differs from the particle size distribution. In order to represent the particle size distribution (26) in the flow field, the parcel size distribution has to be

$$g(D_\mathrm{p}) = \frac{\pi D_\mathrm{p}^2 \rho}{3 m_\mathrm{p} \sqrt{2\pi s^2}} \exp\left(\frac{(\ln D_\mathrm{p}/D_\mathrm{pm})^2}{2s^2} \right) \tag{27}$$

3.4. Interaction of particles with turbulence

In bubbly channel flows, it is observed that big bubbles quickly approach the walls of the channel while moving downstream. Zun (1980) explained this effect with the action of the Magnus and lift forces. However, according to Tran-Cong et al. (1998), the migration to the walls happens in so short time that these forces alone could not be responsible for this motion. It was concluded that turbulence is also very important for this kind of dispersive motion. The effect of turbulence on the particle motion is modelled in the present work by a stochastic procedure. The instantaneous fluid velocity along the particle trajectory is sampled from a Gaussian velocity distribution, with the equal RMS value of $u' = v' = w' = \sqrt{2k/3}$ in all three cartesian co-ordinate directions to simulate isotropic turbulence. The instantaneous fluid velocity is assumed to influence the particle motion during a given time period, called the interaction time, before a new fluctuation component is sampled from the Gaussian distribution function. In the present model, the successively sampled fluid velocity fluctuations are assumed to be uncorrelated. This simulation of the interaction time of a particle with the individual turbulent eddies is governed by two criteria:

(1) The random life times of the turbulent eddies are determined by a Poisson process, where a random variable is sampled from a uniform probability distribution. When this random variable becomes smaller than the ratio $\Delta\tau/T_\mathrm{L}$, where $\Delta\tau$ is the time step and $T_\mathrm{L} = 0.3k/\varepsilon$ is the Lagrangian integral time scale of the turbulence, a new fluctuation is generated. This process results in an exponential form of the particle velocity autocorrelation.

(2) The crossing-trajectory effect is accounted for by integrating the travelling distance of a particle through an eddy and comparing it with the characteristic length scale of the eddy $L_E = T_L u'$. As soon as the particle leaves the eddy, a new fluctuation component is sampled.

In the case of a liquid flow laden with bubbles, the wakes of the bubbles may play an important role for the bubble motion by changing the liquid velocity profile around neighbouring bubbles. This is especially important in cases of small turbulence intensity. Even in the case of laminar flow of a liquid containing bubbles, fluctuations in the liquid phase could arise due to the influence of bubbles. This so-called bubble-induced or pseudo-turbulence results in an additional momentum flux associated with the bubble motion relative to the liquid. In two-fluid models (Euler–Euler approach) the modelling of bubble-induced turbulence is relatively straightforward and can be performed by introducing a bubble-induced counterpart in the stress-level equation, which is then modelled (Lathouwers and Van Den Akker, 1996; Liu and Bankoff, 1993a,b). In the case of Euler–Lagrangian stochastic models there is a problem of taking into account interactions of all possible pairs of bubbles, which is impossible in view of the computation time. The problem could be solved by introducing an additional source term in the liquid momentum equations which accounts for the presence of the disperse phase, but the procedure of connecting the bubble wake with this term is not straightforward. In the present work it was supposed that, due to the fact that the measurements were performed in dilute two-phase and three-phase flows, the pseudo-turbulence was negligible. The modelling of the bubble motion may therefore be less than complete, but most of the results like turbulence levels, which come out of the model, are convincing enough to allow for the conclusion that the effects of the presence of bubbles included in the model are sufficient. Yet, since in our measurements we had no optical access to the entrance region of the flow channel, we have no quantitative information about the bubble distribution there. Therefore, deviations in the bubble effects on the liquid flow between measurement and computation can be interpreted only with some uncertainty. In particular, the contributions from left-out forces and pseudo-turbulence and those from a poor estimation of the real bubble distribution at the entrance of the channel cannot be estimated separately.

4. Experimental and numerical results

Three sets of measurements were carried out in the present work: (1) measurements in the single-phase water flow; (2) measurements in the two-phase flow of water with air bubbles; (3) measurements in the three-phase flow of water with air bubbles and glass particles. Measurements in the single-phase flow were performed for comparison of the water velocity and the turbulence field without and with the presence of disperse phases, and in order to validate the computational model by the experimental results.

The measurements were performed at the three Reynolds numbers $Re = U_e H/\nu = 1500$, 6500, and 13,000, where U_e is the flow-rate equivalent velocity. The flow in the case of $Re = 1500$ clearly belonged to the laminar domain. Although it is hard to find a practical application of such a flow in two-phase systems, it was investigated because the influence of the bubbles on the water velocity profile was clearly obvious only in this case. The bubble influence on the water velocity in the cases of $Re = 6500$ or even $Re = 13{,}000$ would be considerable only for air-to-water volume

ratios above 10%. The PDA measuring technique, however, does not allow disperse phase contents higher than some few percent.

The measurements were performed in three different downstream planes of the channel—at $x/H = 30$, 40, and 50. Measurements at the entrance of the channel were not possible due to limitations in the optical access.

The gas volume concentrations of 0.23%, 0.5% and 0.66% investigated were chosen in order to have conditions similar to previous experiments in a bubble column. The solid concentration is strongly limited by the optical measuring technique. Glass beads with a mean diameter of about 150 μm allow maximum volume concentrations of only 0.054%. Higher concentrations would reduce the data rate for the liquid measurements below acceptable values.

4.1. Single-phase flow

We now present experimental and computational results for the single-phase flow. In Fig. 3a and b the dimensional velocity distributions for the water flow at $x/H = 30$ and $x/H = 50$ are presented for the Reynolds number 1500. For comparison with the theoretical results, the fully developed parabolic profile of the laminar velocity distribution for $Re = 1500$ in the channel is

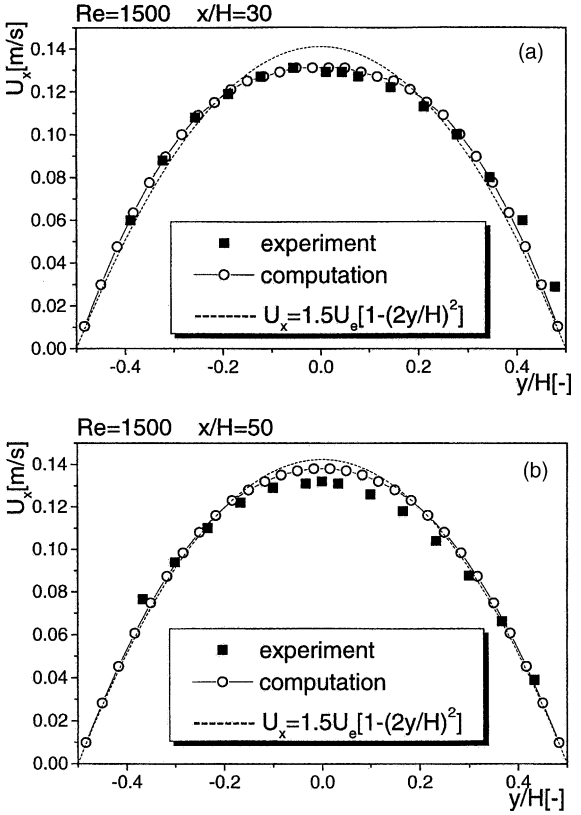

Fig. 3. Water velocity profiles in single-phase flow for $Re = 1500$ at (a) $x/H = 30$ and (b) $x/H = 50$.

also given. In Fig. 3a the difference between the measured and calculated and the parabolic curves is clearly visible, which indicates that the distance of $x/H = 30$ from the channel entrance was not enough for the velocity profile to be developed. The agreement between measured and computed profiles, however, is excellent. With increasing distance x/H the velocity profile develops, and in Fig. 3b we see good agreement between measured and numerical results. The deviation of these two profiles from the parabolic dashed curve in the figure indicates that, even at this downstream position $x/H = 50$, the flow was not fully developed, which is in agreement with the findings of Young and Hanratty (1991). In Fig. 3 and the following figures there is some asymmetry in the measured values between the left and the right-hand sides of the channel, which cannot be explained theoretically. Potentially the aerator was slightly misaligned by an angle of about 0.60° due to manufacturing uncertainties. This would lead to a difference between the mean velocities of the branches of the flow downstream from the aerator body of 4%, which is about the deviation observed.

In Fig. 4 the single-phase water velocity profiles for the three different *Re* numbers in the cross-section $x/H = 50$ are presented. The change of the profiles from the laminar parabolic shape to the turbulent shape with increasing *Re* can clearly be seen. Near the wall, velocities from experiments are slightly higher than the computed values, while in the centre of the channel the agreement is excellent.

As turbulence characteristics of special interest, we consider the Reynolds shear stress $\overline{u'v'}$ and the turbulence intensity. The Reynolds stress is presented in Fig. 5 for the two turbulent values of *Re*. The linear dependence of the Reynolds stress on the transverse co-ordinate y, as well as its growth with increasing *Re* and its zero value at the centre of the channel are clearly visible. The agreement of experimental and computed values is very good; the measured variation with y is slightly smaller than the computed results.

The turbulence intensity profiles for two turbulent *Re* numbers at $x/H = 50$ are drawn in Fig. 6a. The measured x and y velocity fluctuations u' and v' are of the same order in the centre of the channel, but near the walls the fluctuations v' are smaller than u'. We assume that the fluctuations w' in the third spatial direction are very small everywhere in the flow, since the flow is two-dimensional. We therefore disregard w' when calculating the turbulent kinetic energy from the

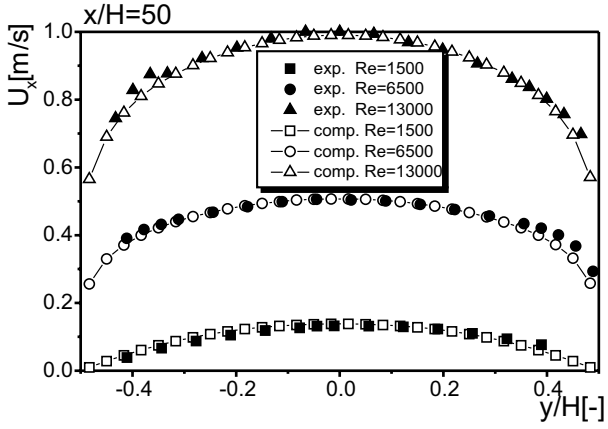

Fig. 4. Water velocity profiles in single-phase flows at $x/H = 50$ for the three values of the Reynolds number (filled symbols—experiment, open symbols—computation).

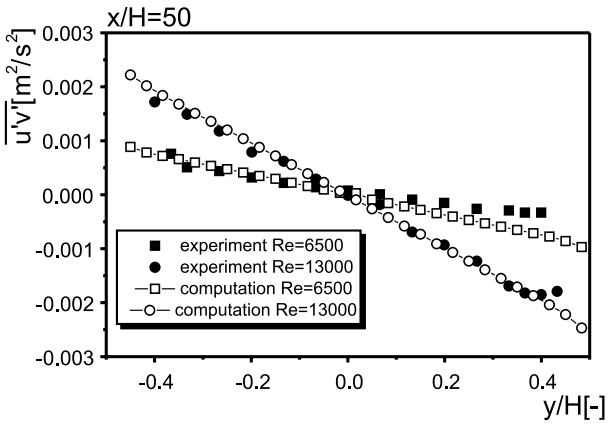

Fig. 5. Mixed Reynolds shear stress in single-phase water flow at $x/H = 50$ for the two turbulent Reynolds numbers (filled symbols—experiment, open symbols—computation).

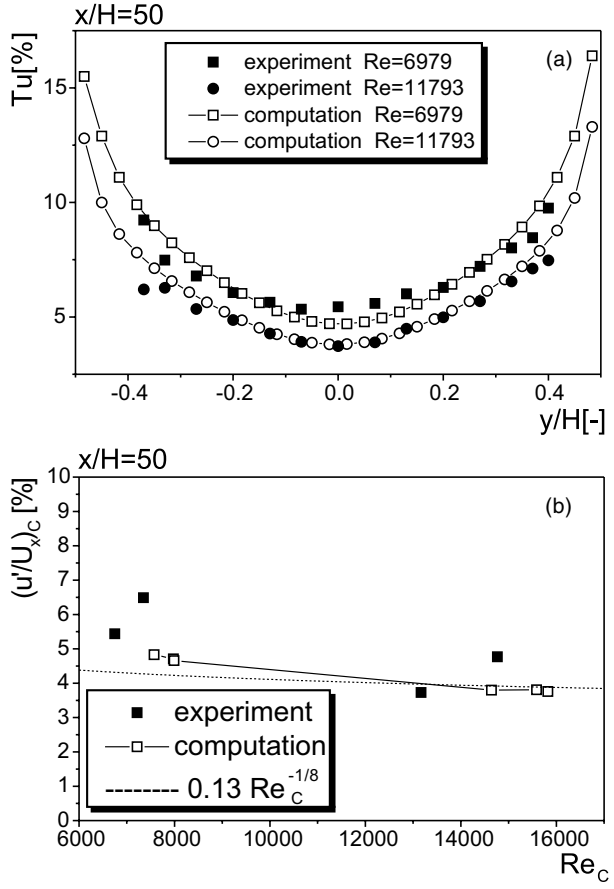

Fig. 6. Turbulence intensity (a) as a function of y/H, and (b) turbulence intensity in the centre of the channel as a function of Re_C ($x/H = 50$).

measurement data. The turbulence intensity derived from the measurements was calculated as $\mathrm{Tu} = \sqrt{2k/3}/U_x$, in accordance with the definition in the k–ε model. Here k is the turbulent kinetic energy $k = 1/2(u'^2 + v'^2)$, and U_x represents the local mean flow velocity in x direction. The agreement of computation and experiment is very good in most parts of the profile; in the near-wall regions the measured Tu is slightly smaller than calculated. The tendency of Tu to decrease with increasing Re is visible. The mild dependence of Tu on Re is even more clearly visible from Fig. 6b, where the turbulence level of the flow at the centre of the channel cross-section is depicted as a function of the above introduced Reynolds number Re_C. From detailed measurements of the turbulence intensity in single-phase channel flows in the range of $3 \times 10^3 < Re_C < 10^5$, Durst et al. (1998) showed that the turbulence level at the centre of the channel cross-section can be well described by the equation $u'/U_c = 0.13 Re_C^{-1/8}$, where the subscript C denotes values at the centre of the channel. This function is also shown in Fig. 6b for reference. It can be seen that both numerical and measurement values are close to the function for all values of Re_C considered.

4.2. Two-phase flow of water with air bubbles

The focus of these measurements was on the (nearly) developed flow. All experiments were therefore performed at the downstream level $x/H = 50$. For the two turbulent flow situations, Re was the same as in the single-phase flow. For the laminar case it was $Re = 1200$.

In bubbly two-phase flows, especially large bubbles migrate towards the walls. Before entering the test section, large bubbles, once they have left the aerator, move more or less straight downstream, i.e. upwards in the present rig. Therefore they reach the entrance of the channel near the walls. Smaller bubbles are more strongly dispersed by the shear flow downstream from the aerator, and therefore they occur in the whole cross-section of the channel. In trying to reproduce computationally the real bubble diameter distribution at the entrance of the test section, which could not be measured there, it was assumed that the concentration of bubbles with diameters less than 600 μm was uniform along the inlet cross-section, and that the diameter of bubbles bigger than 600 μm depends linearly on the inlet y position, so that the biggest bubbles entered the channel closest to the wall.

As a consequence, the strongest effect of bubbles on the water velocity profile is in the regions close to the walls. This is obvious from Fig. 7, where the normalised water velocity profiles in a single-phase and in a bubble-laden case with the gas volume concentration $C_{\mathrm{V,g}} = 0.66\%$ are depicted. Two velocity peaks outside the centre of the channel occur. Antal et al. (1991) computed a laminar bubbly water flow ($Re = 1200$) in a vertical pipe with a finite-element scheme, using a two-equation model (taking into account bubble-induced turbulence), and compared their results with the measurements of Nakoryakov et al. (1986). While in the measurements there was clear peak in the void fraction as well as in the water velocity around $r/R = 0.9$, in the computation only the peak in the void fraction was reproduced. Lopez de Bertodano et al. (1994) made a similar computation for a vertical duct with qualitatively the same result. Considering the water velocity profile, our model showed more sensitivity for the presence of the second phase, although only qualitatively, because the computed distance of the peaks from the centre in our flow is not as big as measured, and the peak heights are about 20% higher in the computation. One possible explanation for this deviation is that the real bubble size distribution at the entrance of the channel does not correspond thoroughly to the one assumed in the computation. On the other

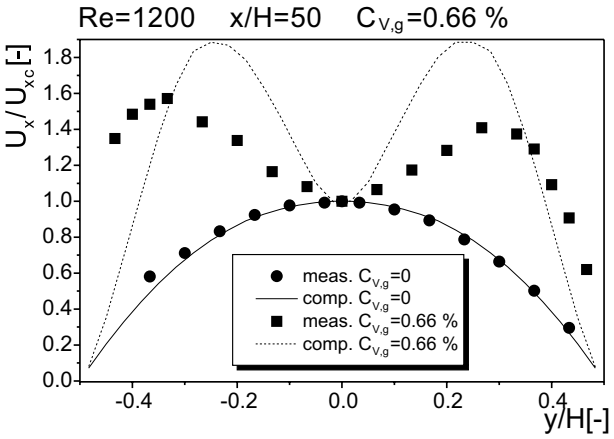

Fig. 7. Normalised water velocity in the two-phase mixture ($Re = 1200$, $x/H = 50$, $C_{V,g} = 0.66\%$).

hand, the agreement of computed and measured mean bubble velocities shown in Fig. 8 is very good. Although the void fraction distribution was not measured, it is indicative that the peak of the bubble velocity coincides with the peak of the void fraction in the measurements of Nakoryakov et al. (1986). In our results, only the region close to the wall exhibits a computed velocity slightly higher than measured. This is due to the fact that in this region the number of bubbles followed in the computation was relatively small, with a predominance of big bubbles, so that the statistically obtained values may be slightly uncertain and systematically overestimated.

The question arises whether it is justified to neglect bubble-induced turbulence in the flow investigated in the present work. In order that it plays an important role, besides a low turbulence level in the water flow it is also necessary that the bubble void fraction is big enough. Lathouwers and Van Den Akker (1996) found that, even in a flow with 5% void fraction with a velocity of 1 m/s and slip velocity of 0.2 m/s (approximately two times larger than in the present work), bubble-induced turbulence in slip direction is only 2%. Laín et al. (1999) studied the flow in a

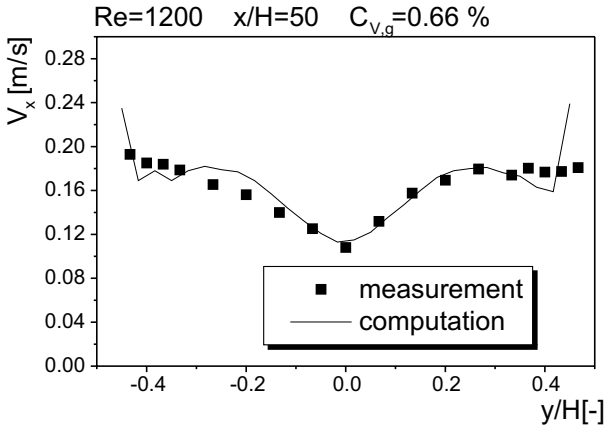

Fig. 8. Bubble mean velocity profile in the two-phase mixture water/bubbles ($Re = 1200$, $x/H = 50$, $C_{V,g} = 0.66\%$).

bubble column numerically with a void fraction of about 1.3%, also neglecting the bubble influence. On the basis of measurements in a pipe, Liu and Bankoff (1993a) derived the dependence $u''/u_f = \alpha^{0.5}$ of the ratio of bubble-induced turbulent fluctuations to the turbulent fluctuations in the liquid on the void fraction α (u'' represents the bubble-induced velocity fluctuations, u_f the liquid velocity fluctuations in the two-phase flow). In the two-phase flow considered in this work, the void fraction was 0.66%, i.e. $u''/u_f = 0.081$. All these examples show that neglecting bubble-induced turbulence is in accordance with the experience of other research groups whose results can be found in the literature.

The difference between the bubble and liquid velocities, i.e. the slip velocity, is given in Fig. 9. The agreement between computation and experiment is qualitatively good, even though the measurements indicate that slip velocities are slightly different at the two sides of the test section. This effect may be caused by different mean bubble sizes on the two sides. The above results were achieved for the smallest *Re* number of 1200.

The influence of the gas phase on the liquid motion is much smaller for bigger *Re*. For $Re = 6500$ it is still visible, but for $Re = 13{,}000$ it almost does not exist, as seen in Fig. 10. The bubble/water velocity ratio for the two turbulent cases is depicted in Fig. 11. The relatively uniform value corresponds to the flat water velocity profile. From Fig. 11a a decrease of the ratio is found in the region where a wall peak of the void fraction is typically detected. The decrease of the water velocity in the vicinity of the wall leads to an enlargement of the ratio in this region. This also indicates that, due to the bubble dispersion induced by turbulence, the bubble size distribution is fairly uniform. This is confirmed by results presented later.

The turbulence intensity Tu is shown in Fig. 12 for the bubble-laden and the pure water flows at the two turbulent *Re* numbers. It is visible that the presence of bubbles damps turbulence. This damping is stronger for $Re = 6500$ than for the higher value of *Re*. The shapes of the *Tu* profiles are similar to those shown in Fig. 6a. Fig. 13 shows the distribution of the volume–average diameter of the bubbles $D_{30.b} = (1/N \sum_{i=1}^{N} D_{i,b}^3)^{1/3}$. In the case of laminar flow, the shape of the size distribution remains very much the same as at the entrance. In the turbulent flows the profiles are rather uniform, which confirms the earlier statement that, for the given range of bubble diameters, turbulence represents the most important factor for bubble dispersion.

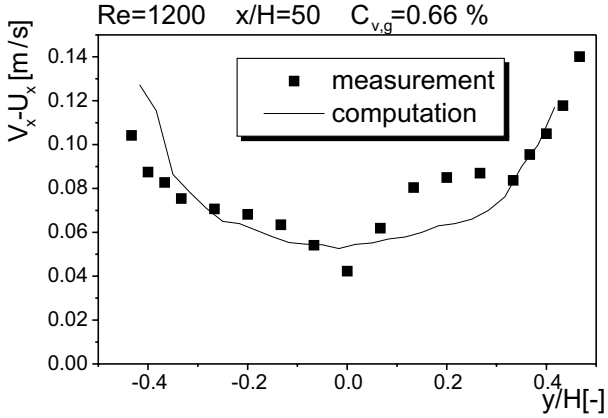

Fig. 9. Difference between bubble and liquid velocity, i.e. slip velocity ($Re = 1200$, $x/H = 50$, $C_{V,g} = 0.66\%$).

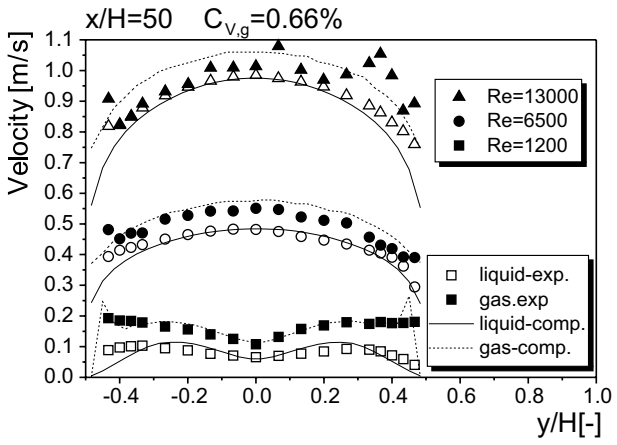

Fig. 10. Profiles of water and bubble velocities U_x and V_x ($x/H = 50$, $C_{V,g} = 0.66\%$).

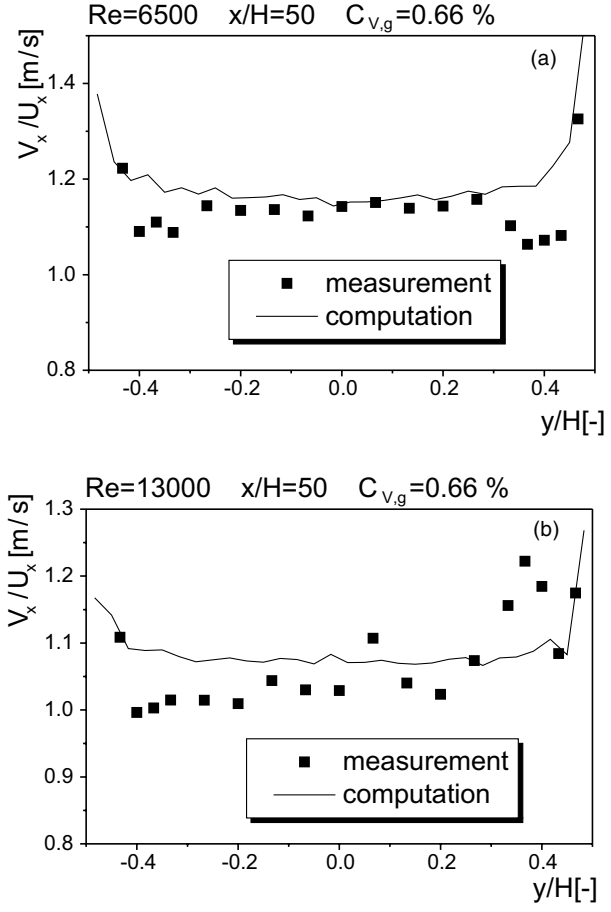

Fig. 11. Ratio of bubble to liquid velocity for (a) $Re = 6500$ and for (b) $Re = 13{,}000$ ($x/H = 50$, $C_{V,g} = 0.66\%$).

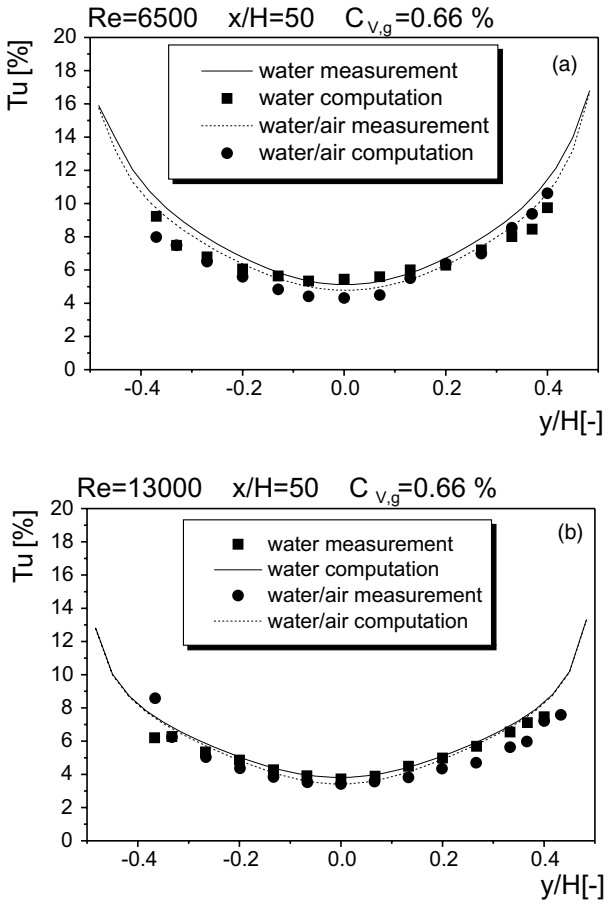

Fig. 12. Turbulence intensity in the two-phase mixture for (a) $Re = 6500$ and for (b) $Re = 13{,}000$ ($x/H = 50$, $C_{V,g} = 0.66\%$).

4.3. Three-phase flow of water with bubbles and glass particles

In the experiments on three-phase flows, the solid particle phase was represented by spherical glass particles. The particle-to-water volume ratio was 0.054%. Due to this small amount of solid phase it was not possible to measure the influence of the solid particles on the water flow, but only the solid particle velocity and concentration distributions. All measurements were performed at $x/H = 50$. For getting reliable average computational values for the particles, 10,000–20,000 parcels were followed, depending on the flow regime.

For the solid particle motion buoyancy is negligible. Accordingly, the particle velocity was lower than the fluid velocity, contrary to the velocity of bubbles. The velocity difference is small, regardless of the value of *Re*, as can be seen in Fig. 14, where the velocity profiles of water and the glass phase are depicted for the *Re* numbers of 6500 and 13,000. This is reasonable, taking into account that the particles are small. Close to the wall, the velocity difference is smaller than in the centre of the cross-section, partly because of the smaller absolute velocities, and partly because of

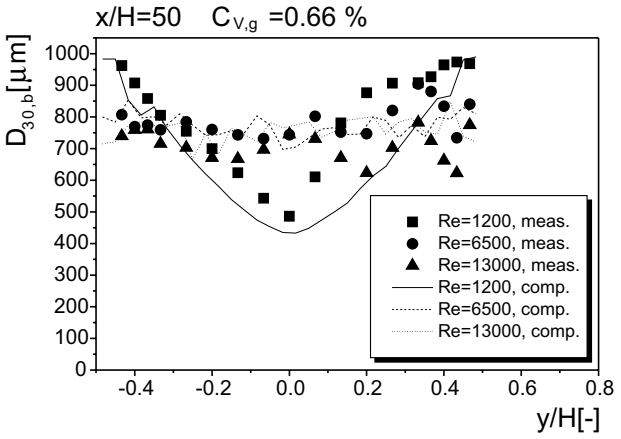

Fig. 13. Distribution of the volume–average bubble diameter in two-phase water/air flows at three different Reynolds numbers ($x/H = 50$, $C_{V,g} = 0.66\%$).

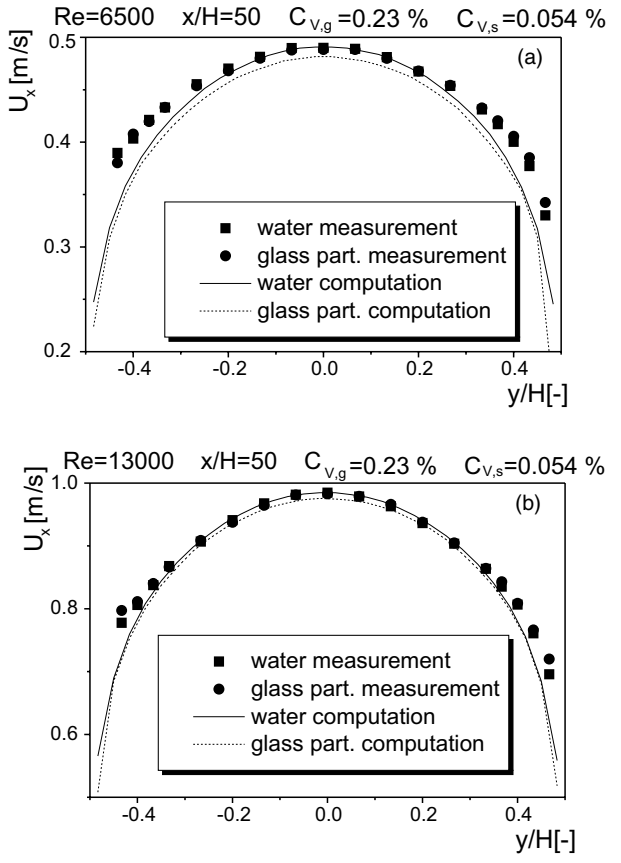

Fig. 14. Water and glass particle velocities in a three-phase flow for (a) $Re = 6500$ and (b) $Re = 13{,}000$ ($x/H = 50$, $C_{V,g} = 0.23\%$, $C_{V,g} = 0.054\%$).

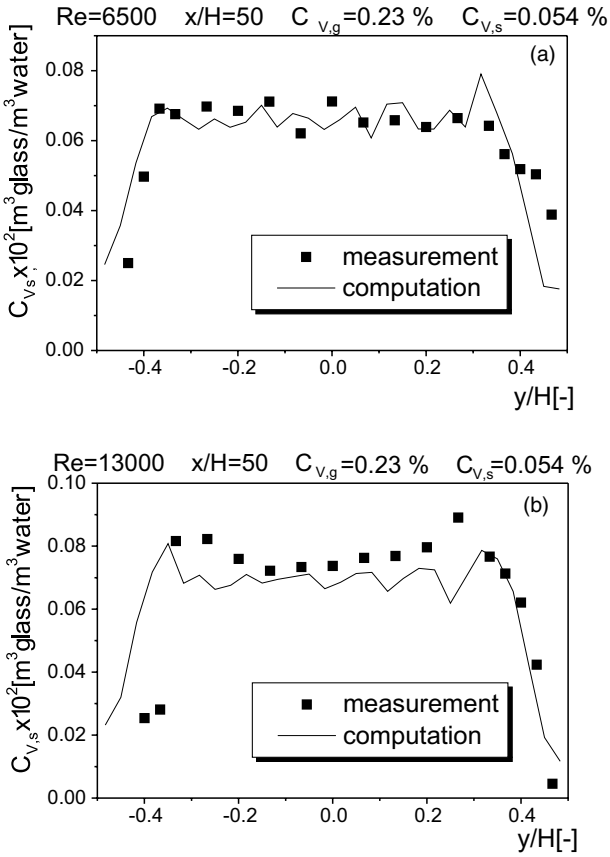

Fig. 15. Glass particles concentration in the three-phase mixture for (a) $Re = 6500$ and for (b) $Re = 13{,}000$ ($x/H = 50$, $C_{V,g} = 0.23\%$, $C_{V,g} = 0.054\%$).

the dispersion of particles from the central part of the channel with larger velocity. The shapes of the profiles are identical. The agreement of experiment and computation is good, especially in the central region of the channel.

Fig. 15 represents the concentration profiles of the solid phase. Taking into account that concentration measurements with PDA are not an easy task, the agreement of experiment and computation is excellent for $Re = 6500$, and good for $Re = 13{,}000$. It is found that the concentration of solid particles decreases rapidly in the vicinity of the wall, while it is uniform in the centre of the channel. For $Re = 13{,}000$, concentration peaks near the wall are observed.

5. Conclusions

Single-, two- and three-phase channel flows with liquid continuous phase were investigated experimentally and simulated numerically using a detailed mathematical model. Measurements were made in a vertical rectangular channel with dimensions chosen such that the flow could be

considered as two-dimensional. For the continuous phase water has been chosen, and the disperse phases were air bubbles and glass particles. The measuring technique was PDA. The walls of the channel were made of smooth glass. The volume fractions of the disperse phases were small, so that mutual collisions of bubbles or solid particles could be neglected in the model.

Due to technical constraints it was not possible to perform measurements at the inlet of the channel. Therefore no information from the measurements on the inlet conditions of the fluid and the disperse phases were available for the computations. An appropriate water velocity profile and bubble size distribution at the entrance were therefore assumed, according to the construction of the aerator and the way bubbles were introduced into the water flow. The presented results show good agreement between the model calculations and experiments. The measured concentration profiles of the disperse phases are excellently reproduced by the calculations. Measured and computed turbulence intensities in the liquid flow agreed well. Both measurements and computations showed an equal effect of water turbulence intensity damping by the bubbles. The influence of the bubbles on the continuous phase is biggest for small *Re*, and it decreases with increasing *Re*. The volume concentration of the glass particles was too small to detect any influence on the water velocity profiles. The influence of liquid on the slip velocity of bubbles increases with increasing Reynolds number. It was shown that water turbulence plays an important role in bubble dispersion.

Acknowledgement

The financial support of this work through grant Du 101/29-2 from the Deutsche Forschungsgemeinschaft is gratefully acknowledged.

References

Ahmad, K., Goulas, A., 1980. A numerical study of the motion of a single particle in a duct flow. In: Proceedings of the 5th International Conference on Pneumatic Transport of Solids in Pipes, London, pp. 75–97.

Antal, S.P., Lahey Jr., R.T., Flaherty, J.E., 1991. Analysis of phase distribution in fully developed laminar bubbly two-phase flow. Int. J. Multiphase Flow 17, 635–652.

Braeske, H., Brenn, G., Domnick, J., 1998a. Detailed investigations of multiphase flows using phase-Doppler anemometry. In: Proceedings of the Third International Conference on Multiphase Flow, ICMF '98, Lyon, France, June 8–12, 1998.

Braeske, H., Brenn, G., Domnick, J., Durst, F., Melling, A., Ziema, M., 1998b. Extended phase-Doppler anemometry for measurements in three-phase flows. Chem. Eng. Technol. 21, 415–420.

Brenn, G., Durst, F., Melling, A., Xu, T.H., Ziema, M., 1994. Development of improved PDAs for multiphase flows. In: Proceedings of the German–Japanese Symposium on Multiphase Flow, Karlsruhe, August 23–25, 1994, pp. 67–79.

Clift, R., Grace, J.R., Weber, M.E., 1978. Bubbles, Drops and Particles. Academic Press, New York.

Crowe, C.T., 1981. On the relative importance of particle–particle collisions in gas-particle flows. In: Proceedings of the Conference on Gas-Borne Part, paper C78/81, pp. 135–137.

Crowe, C.T., Sharma, M.P., Stock, D.E., 1977. The Particle-Source-in-Cell (PSI-CELL) model for gas-droplet flows. J. Fluids Eng. 99, 325–332.

Durst, F., Fischer, M., Jovanovic, J., Kikura, H., 1998. Methods to set up and investigate low Reynolds number, fully developed turbulent plane channel flows. J. Fluids Eng. 120, 496–503.

Durst, F., Raszillier, H., 1989. Analysis of particle–wall interaction. Chem. Eng. Sci. 44, 2872–2879.

Durst, F., Milojevic, D., Schönung, B., 1984. Eulerian and Lagrangian predictions of particulate two-phase flows: a numerical study. Appl. Math. Modelling 8, 101–115.

Felton, K., Loth, E., 1998. Bubbly flow in a vertical turbulent boundary layer. In: Proceedings of the 3rd International Conference Multiphase Flow, ICMF'98, Lyon, France, June 8–12, 1998.

Hardalupas, Y., Moreira, A.L.N., Taylor, A.M.K.P., Whitelaw, J.H., 1995. Evaluation of the phase-Doppler technique for the measurement of bubbles. In: Proceedings of the 2nd International Conference on Multiphase Flow 95, Kyoto, April 3–7, 1995, pp. 1–8.

Hetsroni, G., 1989. Particles–turbulence interaction. Int. J. Multiphase Flow 15, 735–746.

Hinze, J.O., 1975. Turbulence, 2nd ed. McGraw-Hill, New York.

Kashinsky, O.N., Timkin, L.S., 1999. Slip velocity measurements in an upward bubbly flow by combined LDA and electrodiffusional techniques. Exp. Fluids 26, 305–314.

Lahey Jr., R.T., 1990. The analysis of phase separation and phase distribution phenomena using two-fluid models. Nucl. Eng. Design 122, 17–40.

Laín, S., Bröder, B., Sommerfeld, M., 1999. Numerical studies of the hydrodynamics in a bubble column using the Euler–Lagrange approach. In: Proceedings of the 9th Workshop on Two-Phase Flow Predictions, Merseburg (Germany), April 13–16, pp. 242–251.

Lathouwers, D., Van Den Akker, H., 1996. An evaluation of two-fluid models for two-phase turbulent bubbly flows. In: Proceedings of the 8th Workshop on Two-Phase Flow Predictions, Merseburg (Germany), March 26–29, pp. 71–84.

Launder, B.E., Spalding, D.B., 1974. The numerical computation of turbulent flows. Comput. Methods Appl. Mech. Eng. 3, 269–289.

Lee, S.L., Durst, F., 1982. On the motion of particles in turbulent duct flows. Int. J. Multiphase Flow 8, 125–146.

Lee, S.L., Yang, Z.H., 1989. Measurement of size and two velocity components of large bubbles and particles and velocity of carrier phase in a three-phase suspension flow by laser-Doppler anemometry. In: Proceedings of the International Conference on Mechanics of Two-Phase Flows, June 12–15, 1989, Taipei, Taiwan, pp. 97–102.

Liu, T.J., Bankoff, S.G., 1993a. Structure of air–water bubbly flow in a vertical pipe—I. Liquid mean velocity and turbulence measurements. Int. J. Multiphase Flow 36, 1049–1060.

Liu, T.J., Bankoff, S.G., 1993b. Structure of air–water bubbly flow in a vertical pipe—II. Void fraction, bubble velocity and bubble size distribution. Int. J. Multiphase Flow 36, 1061–1072.

Lopez de Bertodano, M., Lahey Jr., R.T., Jones, O.C., 1994. Phase distribution in bubble two-phase flows in vertical ducts. Int. J. Multiphase Flow 20, 805–818.

Matsumoto, S., Saito, S., 1970a. Monte Carlo simulation of horizontal pneumatic conveying based on the rough wall model. J. Chem. Eng. Jpn. 3, 223–230.

Matsumoto, S., Saito, S., 1970b. On the mechanism of suspension of particles in horizontal pneumatic conveying: Monte Carlo simulation based on the irregular bouncing model. J. Chem. Eng. Jpn. 3, 83–92.

Migdal, D., Agosta, V.D., 1967. A source flow model for continuum gas-particle flow. Trans. ASME 34, 860–865.

Milojevic, D., 1990. Lagrangian stochastic–deterministic (LSD) prediction of particle dispersion in turbulence. Part. Part. Syst. Charact. 7, 181–190.

Mostafa, A.A., Elghobashi, S.E., 1985. A two-equation turbulence model for JET flows laden with vaporising droplets. Int. J. Multiphase Flow 11, 515–533.

Nakoryakov, V.E. et al., 1986. Study of upward bubbly flow at low liquid velocities. Izv. Sib. Otdel. Akad. Nauk SSSR 16, 15–20.

Nakoryakov, V.E., Kashinsky, O.N., 1995. Gas–liquid bubbly flow in a near-wall region. In: Proceedings of the International Symposium on Two-Phase Flow Modelling and Experimentation, Rome, October 9–11, 1995, pp. 453–457.

Odar, F., Hamilton, W.S., 1964. Forces on a sphere accelerating in a viscous fluid. J. Fluid Mech. 18, 302–314.

Oesterle, B., Petitjean, A., 1993. Simulation of particle-to-particle interaction in gas–solid flows. Int. J. Multiphase Flow 19, 199–211.

Patankar, S.V., 1980. Numerical Heat Transfer and Fluid Flow. Hemisphere, New York.

Rubinow, S.I., Keller, B., 1961. The transverse force on a spinning sphere moving in a viscous fluid. J. Fluid Mech. 11, 447–459.

Saffman, P.G., 1965. The lift on a small sphere in a shear flow. J. Fluid Mech. 22, 385–400.

Serizawa, A., Kataoka, I., 1987. Phase distribution in two-phase flow. Transient phenomena in multiphase flow. In: ICHMT Proc. vol. 26, International Seminar 1987, pp. 179–224.

Sheng, Y.Y., Irons, G.A., 1991. A combined laser-Doppler anemometry and electrical probe diagnostics for bubbly two-phase flow. Int. J. Multiphase Flow 17, 585–598.

Sommerfeld, M., 1987. Expansion of a gas–particle mixture in a supersonic free jet flow. Z. Flugwiss. Weltraumforsch. 11, 87–96.

Sommerfeld, M., Zivkovic, G., 1992. Recent advances in the numerical simulation of pneumatic conveying through pipe systems. In: Computational Methods in Applied Science, Invited Lectures and Special Technological Sessions of the First European Computational Fluid Dynamics Conference, Brussels, pp. 201–212.

Tsuji, Y., Oshima, T., Morikawa, Y., 1985. Numerical simulation of pneumatical conveying in a horizontal pipe. KONA 3, 38–51.

Tran-Cong, S., Marié, J.L., Perkins, R.J., 1998. Experimental study of the bubble motion in an upward turbulent boundary layer. In: Proceedings of the 3rd International Conference on Multiphase Flow (ICMF'98), Lyon (France), June 8–12, 1998, pp. 1–8.

Vassallo, P.F., Kumar, R., 1999. Liquid and gas velocity measurements using LDV in an air–water duct flow. Exp. Thermal Fluid Sci. 19, 85–92.

Vassallo, P.F., Trabold, T.A., Moore, W.E., Kirouac, G.J., 1993. Measurements of velocities in gas–liquid two-phase flow using laser Doppler velocimetry. Exp. Fluids 15, 227–230.

Velidandla, V., Putta, S., Roy, R.P., 1996. Velocity field in isothermal turbulent bubbly gas–liquid flow through a pipe. Exp. Fluids 21, 347–356.

Young, J.B., Hanratty, T.J., 1991. Optical studies on the turbulent motion of solid particles in a pipe flow. J. Fluid Mech. 231, 665–688.

Živković, G., 1996. Mathematical modelling of two-phase gas-particle flow in horizontal tubes and channels. PhD Dissertation, University of Belgrade.

Zun, I., 1980. The transverse migration of bubbles influenced by walls in vertical bubbly flows. Int. J. Multiphase Flow 6, 583–588.